

## Full Length Article

Synergetic effect of interface and surface on photocatalytic performance of TiO<sub>2</sub>@ hollow CeO<sub>2</sub> core-shell nanostructuresYi-Che Chen<sup>a</sup>, Yu-Cheng Chang<sup>a</sup>, Alexandre Gloter<sup>b</sup>, Pei-Kai Hsu<sup>a</sup>, Jenn-Ming Song<sup>c</sup>, Shih-Yun Chen<sup>a,\*</sup><sup>a</sup> Department of Materials Science and Engineering, National Taiwan University of Science and Technology, Taipei, Taiwan<sup>b</sup> Laboratoire de Physique des Solides, CNRS, Université Paris-Saclay, Orsay, 91405, France<sup>c</sup> Department of Materials Science and Engineering, National Chung Hsing University, Taichung, Taiwan

## ARTICLE INFO

## Keywords:

Core shell structure  
Interface  
Surface  
STEM/EELS  
Photocatalyst  
Defect

## ABSTRACT

The photocatalytic performance of new TiO<sub>2</sub>/CeO<sub>2</sub> composites is reported and the mechanism for its enhancement with respect to bare TiO<sub>2</sub> and CeO<sub>2</sub> nanoparticles is revealed. With a two-step process, TiO<sub>2</sub> shells were deposited on CeO<sub>2</sub> hollow cores forming the composites (TiO<sub>2</sub>@H-CeO<sub>2</sub>). With tuning the shell deposition, optical properties were engineered. The absorption range was extended to visible light and the lifetime of photo-induced electron-hole pairs were prolonged. Photo-degradation experiments indicate that the removing of 10<sup>-5</sup> M methylene blue by TiO<sub>2</sub>@H-CeO<sub>2</sub> was improved under both UV and visible light. The highest degradation rate constant *K* reached 0.023 min<sup>-1</sup> under visible light showing an enhancement of more than one order of magnitude as compared to solely TiO<sub>2</sub> or CeO<sub>2</sub> nanoparticles. High-resolution electron energy loss spectroscopy was utilized to investigate both surface and interface areas. It demonstrates a strong interface interaction between CeO<sub>2</sub> and TiO<sub>2</sub> after forming core-shell structure with the introduction of a nanometrical interface layer and a modification of the Ce<sup>3+</sup> and Ti<sup>3+</sup> content near the interface. The present work revealed that the photocatalytic efficiency can be improved effectively by optimizing the synergistic effect of interface through adjusting the TiO<sub>2</sub> deposition process.

## 1. Introduction

CeO<sub>2</sub> was reported as an efficient photocatalyst owing to the high oxygen storage capacity, unique reversible redox reaction between Ce<sup>3+</sup> and Ce<sup>4+</sup> [123] and high resistance to photocorrosion [45]. Besides, it is eco-friendly and with high stability. The disadvantage of CeO<sub>2</sub> in photocatalytic application comes from its intrinsic wide bandgap which restrains the utilization of solar energy. In order to extend the utilization of visible light, various methods have been used. Doping 3d-transition metal or 4f rare earth element to decrease the bandgap of a semiconductor photocatalyst is the first approach. The resultant lattice defects could act as recombination center [6] and the change in electronic structure could also enhance the absorption of visible light [7]. Another favorable method to enhance its photo activity is the decoration of noble metal (e.g., Au and Ag) nanoparticles on the surface. The localized surface plasmon resonance (LSPR) of noble metal nanoparticles was evident to extend light response range [89]. Upon being excited by visible light, photo induced electrons transferred immediately from

these metal particles to the conduction band of CeO<sub>2</sub>. The resultant electron-deficient noble metals would oxidize organic pollutants directly, which were then reduced to their original state. [10]

In recent years, composite formation and surface photosensitization were proposed to further improve catalytic performance. In CeO<sub>2</sub>-based composites, the modification of CeO<sub>2</sub> by combining with TiO<sub>2</sub> is a good strategy. TiO<sub>2</sub> is the most widely discussed photocatalyst material because of its non-toxicity and high chemical stability. However, TiO<sub>2</sub> has several disadvantages such as wide band gap and fast recombination rate of charge carriers. Some previous studies showed that after doping Ce into TiO<sub>2</sub>, the light absorption range can be extended to visible light region as well as the higher photocatalytic activity [111213]. Lots of effort has been made to develop CeO<sub>2</sub>-TiO<sub>2</sub> composites for photocatalytic oxidation of organic pollutants. The improved photocatalytic performance of CeO<sub>2</sub>-TiO<sub>2</sub> composites could be attributed to the formation of interface. Tian et al. demonstrated the deposition of CeO<sub>2</sub> on the TiO<sub>2</sub> nanobelt, [14] in which the rate of charge carrier recombination can be inhibited due to band structure matching after forming

\* Corresponding author.

<https://doi.org/10.1016/j.apsusc.2021.150602>

Received 26 May 2021; Received in revised form 2 July 2021; Accepted 8 July 2021

Available online 24 July 2021

0169-4332/© 2021 Elsevier B.V. All rights reserved.

hetero-structure. Muñoz-Batista et al. reported that, not only forming hetero-structure, but also the appearance of  $\text{Ce}^{3+}$  is helpful to suppress the recombination of electron-hole pairs [15].

Among  $\text{CeO}_2$  based composites, core-shell structures which comprises two or more kinds of substances have attracted much attention [16-19]. Chen et al. [20] reported the synthesis of  $\text{CeO}_2@\text{TiO}_2$  core-shell composites with a facile hydrothermal method. The degradation rate was  $0.012 \text{ min}^{-1}$ , which was 3 and 4 times higher than those of bare  $\text{CeO}_2$  ( $0.004 \text{ min}^{-1}$ ) and  $\text{TiO}_2$  ( $0.003 \text{ min}^{-1}$ ), respectively. Furthermore, hollow structure has been applied to further improve the catalytic performance. Hollow structure is featured by its low density and high surface area that provide more active sites at the surface. Composites made of hollow structure were supposed to promote the charge separation as well as the photocatalytic performance. Up to now,  $\text{CeO}_2@$ -hollow  $\text{TiO}_2$  [16 21] and  $\text{TiO}_2@$ hollow  $\text{CeO}_2$  [22] both have been synthesized successfully. Zhang et al. [23] prepared a hollow  $\text{CeO}_2@$ - $\text{TiO}_2$  composite with a core-shell structure by precipitation combining hydrothermal method. The optical capacity of  $\text{CeO}_2/\text{TiO}_2$  hybrid catalyst showed a visible light absorbance with a band edge ca. 500 nm. The degradation of RhB by  $\text{CeO}_2/\text{TiO}_2$  composites was 75% within 3 h.

Though various hollow  $\text{CeO}_2@\text{TiO}_2$  composite demonstrated promising photocatalytic performance, the enhancement of photocatalytic performance was attributed to charge transform efficiency facilitated by its core-shell structure. But there are still few reports on the microstructure analysis of the interface of such composite materials. In these core-shell structure composite, the structural changes at the interface and the interaction between the two oxides should play an important role in the improvement of photocatalytic properties. In this study, a simple two step method was developed to prepare hollow core-shell structure composites. The interface structures were investigated by electron microscopy and electron energy loss spectroscopy. Photocatalyst performance was improved with adjusting the interface interactions. As using methylene blue (MB) as the dye, the rate constant  $K$  was enhanced to  $0.1 \text{ min}^{-1}$  and  $0.023 \text{ min}^{-1}$  under UV and visible light respectively.

## 2. Experimental procedure

### 2.1. Preparation of H-CeO<sub>2</sub>

Hollow  $\text{CeO}_2$  microspheres were prepared using spray pyrolysis (SP) method. Ceric ammonium nitrate ( $\text{CeAN}$ ,  $(\text{NH}_4)_2\text{Ce}(\text{NO}_3)_6$ , 99.5%, Alfa Aesar) and glycine (GN,  $\text{C}_2\text{H}_5\text{NO}_2$ , 98%, Acros Organics) as the precursor were dissolved in deionized water with molar ratio 4 : 6. The solution was atomized into small droplets at first (nebulizer, King Ultronics Co., Ltd, Taipei, Taiwan) and went through  $350^\circ\text{C}$ ,  $650^\circ\text{C}$  and  $250^\circ\text{C}$  under atmosphere in a heated tubular reactor. Finally, hollow  $\text{CeO}_2$  microspheres were collected using a cylindrical electrostatic collector with high voltage potential.

### 2.2. Preparation of $\text{TiO}_2@$ H-CeO<sub>2</sub> core-shell structure

The deposition of  $\text{TiO}_2$  nanoparticles on hollow  $\text{CeO}_2$  microspheres was carried out by sol-gel method. 20 mg hollow  $\text{CeO}_2$  microspheres were dispersed in 30 ml isopropanol mixed with appropriate amount of titanium isopropoxide (TTIP) and anhydrous ethanol and stir for 2 h followed by adding 1 ml deionized water and 5 ml ethanol. The mixture was stirred for another 24 h and then washed by deionized water and ethanol. The precipitate was dried under  $80^\circ\text{C}$  for 24 h and annealed at  $450^\circ\text{C}$  for 2 h to get  $\text{TiO}_2@$ H-CeO<sub>2</sub> core-shell structure. Samples were named as Ce-3Ti, Ce-4Ti, Ce-5Ti and Ce-7Ti according to the molar ratio between Ti and Ce.  $\text{TiO}_2$  nanoparticles were prepared by the same procedure without adding hollow  $\text{CeO}_2$  microspheres.

## 2.3. Characterization

Crystal structure of all samples were characterized by using X-ray powder diffractometer (XRD) with  $\text{Cu K}\alpha$  radiation (Bruker D2 PHASER XE-T XRD). The morphologies and elemental mapping were studied using transmission electron microscopy (TEM) with accelerate voltage to be 200 keV (FEI Tecnai™ G2 F-20 S-TWIN, FEI Talos F200XG2). The STEM-EELS was done with a Nion STEM microscope operated at 100 keV. EELS valence quantification were done by fitting the Ti-L and Ce-M edges with references spectra (anatase  $\text{TiO}_2$  and  $\text{DyTiO}_3$  for  $\text{Ti}^{4+}/\text{Ti}^{3+}$ , fluorite  $\text{CeO}_2$  and  $\text{CeAl}_2$  for  $\text{Ce}^{4+}/\text{Ce}^{3+}$ ). To allow interface observation, nanoparticles were embedded and cut by ultramicrotome. The X-ray absorption measurement was carried at the National Synchrotron Radiation Research Center (NSRRC), Taiwan. Ce  $L_3$ -edge was performed at a DCM tender X-ray beamline 16A with energy resolution set to 0.25 eV. Ti- $L_{2,3}$  edge and Ce  $M_{4,5}$  edge were recorded at HSGM beamline 20A and the energy resolution was about 0.017 eV and 0.01 eV respectively. The optical properties including UV-Vis spectra and photoluminescence spectra were measured by UV-VIS/NIR spectrophotometer (Jasco V-670) and Jasco FP-6300 spectrofluorometer.

## 2.4. Photocatalytic activity

MB with concentration  $10^{-5} \text{ M}$  was used to evaluate the photocatalyst performance of  $\text{TiO}_2$  NPs, H-CeO<sub>2</sub> and  $\text{TiO}_2@$ H-CeO<sub>2</sub> composite. The samples (50 mg) were mixed with dye solution (50 ml) and stirred for 30 min in dark condition first then illuminated with UV light or visible light. For UV light irradiation, a 400 W mercury lamp with  $\lambda_{\text{max}} = 365 \text{ nm}$  was used as the light source. For visible light irradiation, a 300 W sunlight simulated lamp with radiation wavelength from 380 to 780 nm was applied. Within every 10 min (UV light) or 20 min (visible light), about 3 ml of the mixed solution was taken out and filtered for the absorbance investigation. The absorbance of the MB was measured with a UV-VIS/NIR spectrophotometer.

## 3. Results and discussion

### 3.1. Microstructures of hollow core-shell composites

X-ray diffraction spectra of  $\text{TiO}_2@$ H-CeO<sub>2</sub> with different ratios of Ti/Ce are shown in Fig. S1. XRD results of  $\text{TiO}_2$  nanoparticles prepared by using the same process as well as bare  $\text{CeO}_2$  hollow spheres (H-CeO<sub>2</sub>) were plotted together. The observed peaks can be attributed to  $\text{CeO}_2$  cubic fluorite structure (JCPDS 34-0394) and anatase  $\text{TiO}_2$  phase (JCPDS 21-1272). The absence of extra peaks predicts that there are no crystallite impurities within the detection limit. In addition, intensity of characteristic peaks of anatase  $\text{TiO}_2$  is enhanced with increasing amount of Ti precursor (TTIP), confirming the increment of  $\text{TiO}_2$  content.

TEM images of  $\text{TiO}_2@$ H-CeO<sub>2</sub> with different Ti/Ce ratio are illustrated in Fig. 1 (a-d). Two phases were observed. The first is large hollow sphere. As shown in Fig. S2, the diameter ranges from 100 nm to  $2 \mu\text{m}$ . The second is nanoparticle with size ranges between 5 and 10 nm. As the Ti/Ce ratio increases, the amount and coverage of nanoparticles on the surface of the hollow spheres increase, thus forming composites with different morphologies. In Ce-3Ti (Fig. 1 (a)) and Ce-4Ti (Fig. 1 (b)), there are few particles on the surface. In Ce-5Ti (Fig. 1 (c)), the large sphere was fully covered by nanoparticles. The thickness of the shell is about 30 nm. In Ce-7Ti (Fig. 1 (d)), the shell thickness formed by nanoparticles reaches 50 nm. In addition, clusters outside the composites were observed. Microstructure of both phases was then determined. Ce-5Ti was taken as an example. The selected area diffraction pattern of the core-shell structure was shown in Fig. 1 (e). The rings were corresponded to  $\text{TiO}_2$  (1 0 1),  $\text{CeO}_2$  (1 1 1),  $\text{CeO}_2$  (2 0 0), and  $\text{CeO}_2$  (2 2 0), respectively. High resolution TEM image of the selected area is shown in Fig. 1 (f), indicating that the nanoparticles are with high crystallinity. The lattice spacing equals to 0.352 nm, which can be assigned to  $\text{TiO}_2$  (1

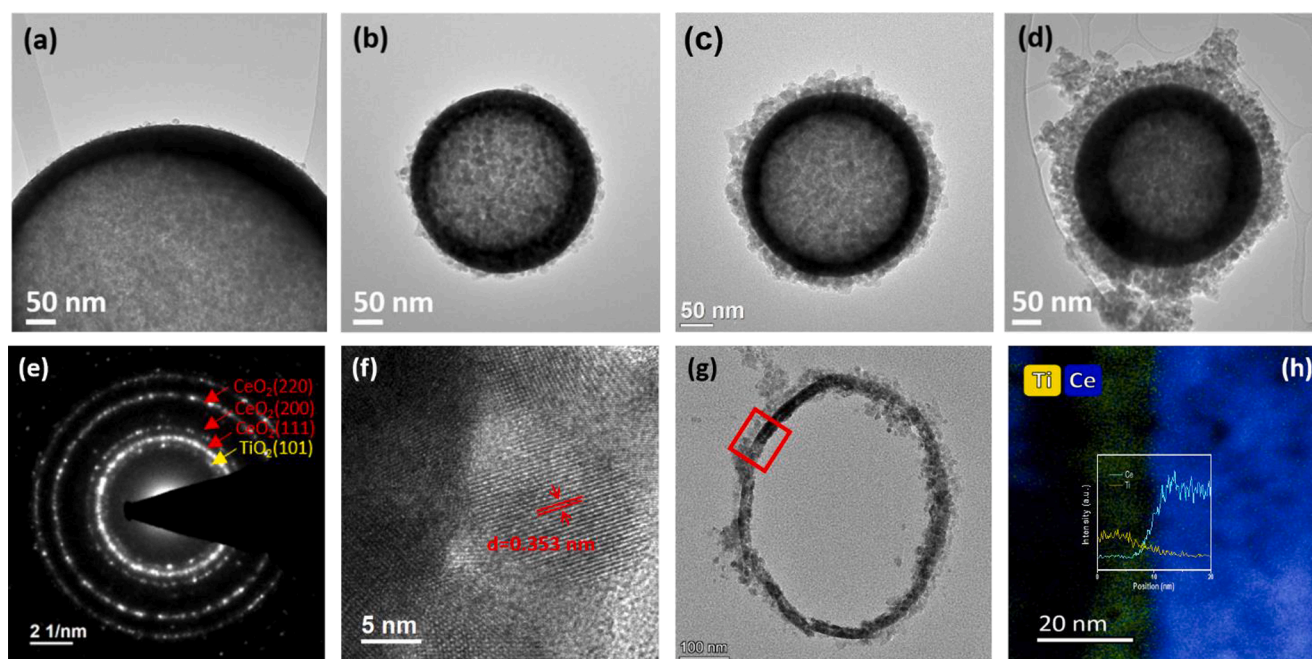


**Fig. 1.** TEM images of  $\text{TiO}_2$ @H- $\text{CeO}_2$  with different Ti/Ce ratio, (a) Ce-3Ti, (b) Ce-4Ti, (c) Ce-5Ti. (d) Ce-7Ti. Detailed observation of Ce-5Ti. (e) Diffraction pattern of the selected area. (f) High-resolution TEM image of shell. (g) Cross-sectioned TEM image. (h) EDS mapping of Ti and Ce obtained from the red square marked region. Intensity profile of Ce and Ti was plotted together.

0 1). Cross sectional TEM result is shown in Fig. 1 (g), confirming that the composite is made of a hollow sphere with nanoparticles on the surface. Element mapping of Ti and Ce was carried out on the marked red square. The mapping result and the line profile confirm the composition of both the  $\text{CeO}_2$  sphere and the  $\text{TiO}_2$  shell (Fig. 1 (h)).

The interfacial structures was investigated by utilizing STEM-EELS with high spatial resolution. Ce-3Ti was studied at first. The results are shown in Fig. 2, where the  $\text{CeO}_2$  core is clearly visible with white contrast and small amount of NPs are present on the surface. EELS mapping based on the Ti-L and Ce-M edges reveals that in addition to the  $\text{TiO}_2$  particles, a thin titanium rich oxide layer is present on the surface of  $\text{CeO}_2$  (Fig. 2 (c)). This layer is typically 1 nm thick, in which Ce and Ti are strongly mixed, and the ratio of Ce to Ti reaches 1.8 to 2.4. This

surface layer is found to be discontinuous, but seems to be always present underneath  $\text{TiO}_2$  NPs. EELS spectra extracted at the surface layer (spectrum 1) shows that the electronic structure is different from the  $\text{TiO}_2$  NPs (spectrum 2) and  $\text{CeO}_2$  core (spectrum 3). In addition, it shows that Ti does not diffuse into the bulk region of the  $\text{CeO}_2$  core (spectrum 3).

STEM and EELS Ce-M edges for Ce-5Ti is shown in Fig. 3. For this sample, the surface layer is found to be continuous, with  $\text{TiO}_2$  NPs consistently grown on top of it. In addition, a clear difference between the outside and inner surface of the  $\text{CeO}_2$  shell is evident. At the outside surface, a large amount of  $\text{Ce}^{3+}$  at the interface layer was found (up to 60%  $\text{Ce}^{3+}/\Sigma\text{Ce}$  as quantified by EELS, see quantification profiles in Fig. S3). A small gradient of  $\text{Ce}^{3+}$  from this interface toward the center of

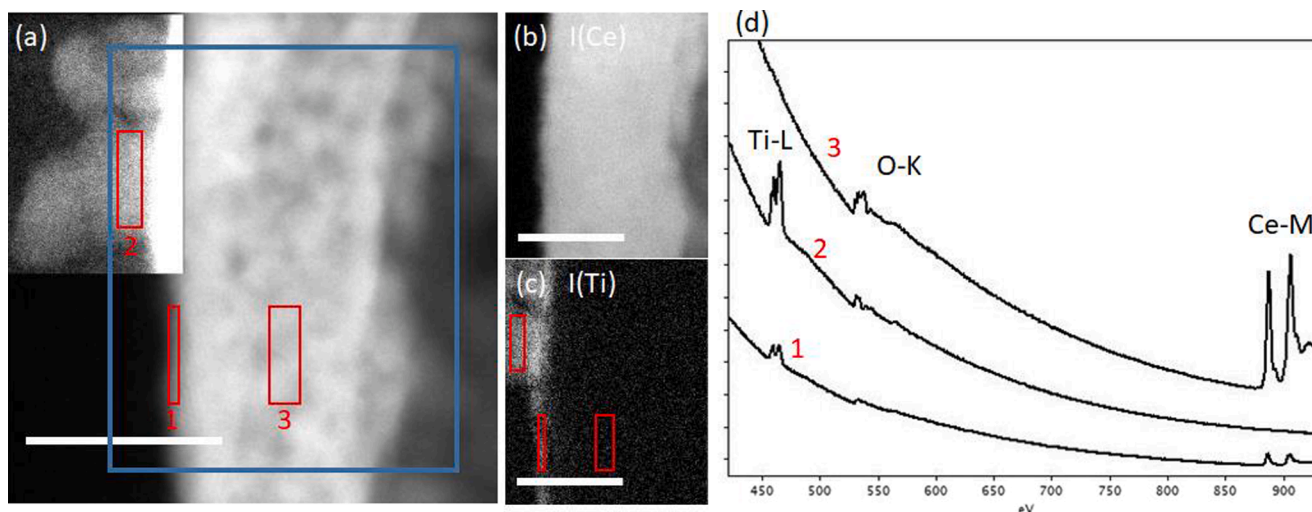


**Fig. 2.** (a) STEM-HAADF image of Ce-3Ti. The contrast have been changed in the upper left part to enable nanoparticles visualization at the surface. The blue box indicates the area for EELS spectromicroscopy. The red boxes indicates positions where spectra have been extracted. (b, c) intensity of the EELS Ti-L and Ce-M edges, (d) EELS spectra extracted from the red boxes. Boxes 1,2,3 are from the surface layer, the nanoparticle at the surface and the central part of the  $\text{CeO}_2$ . All scale bars are 20 nm long.

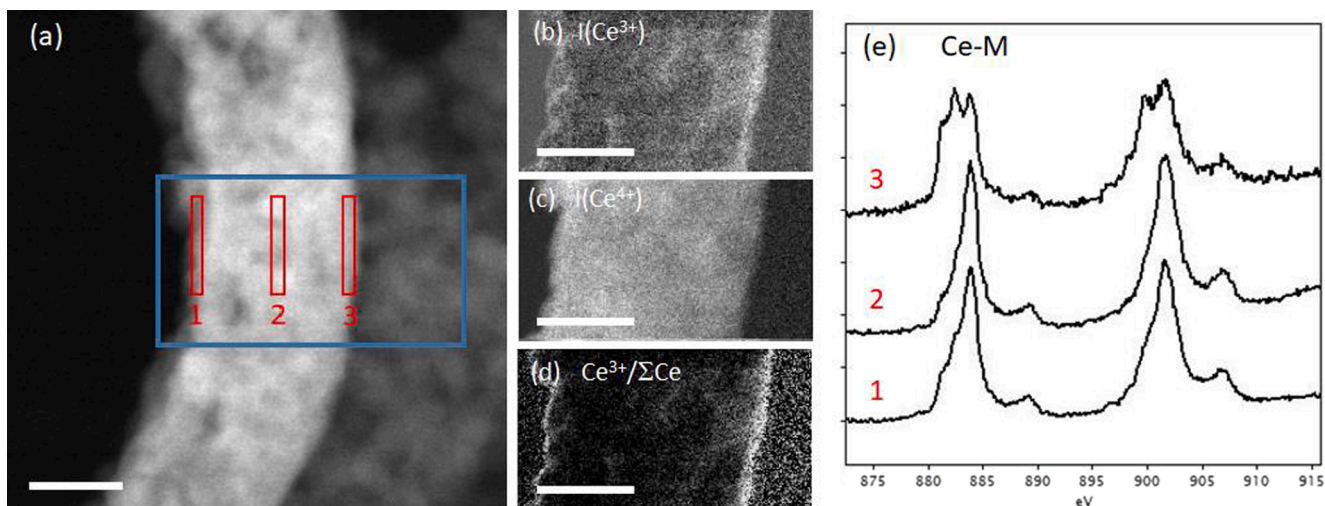


**Fig. 3.** (a) STEM-HAADF image of Ce-5Ti. The blue box indicates the area for EELS spectromicroscopy. The red boxes indicates positions where spectra have been extracted. (b, c, d) intensity of the EELS  $\text{Ce}^{3+}$ ,  $\text{Ce}^{4+}$  and  $\text{Ce}^{3+}/\Sigma\text{Ce}$  edges, (e) EELS Ce-M edges extracted from the red boxes. Boxes 1,2,3 are from the inner surface, central part and outer surface of the  $\text{CeO}_2$ . All scale bars are 20 nm long.

the  $\text{CeO}_2$  is also shown, where an almost pure  $\text{Ce}^{4+}$  can be observed (spectrum 2). However, at the inner surface, the contribution of the  $\text{Ce}^{3+}$  is almost restrained to the surface plane and integrating over ca. 1.5 nm shows mostly a  $\text{Ce}^{4+}$  spectrum (spectrum 1).

EELS Ti-L and O-K edges for Ce-5Ti are presented in Fig. 4. Clearly, the distribution of  $\text{Ti}^{3+}$  is rather inhomogeneous. EELS spectra for NPs located at the most outside part of the  $\text{TiO}_2$  shell have more resolved Ti-L edges fine structure (spectrum 4), which is compatible with anatase (shape / shoulder position of the so called “Ti- $L_3$   $e_g$ ” peak [24]). Getting closer to the  $\text{CeO}_2$  core (spectrum 3), the NPs have broader Ti-L fine structure that is primary due to a larger  $\text{Ti}^{3+}$  contribution while some structural contribution from more defect cannot be totally excluded in the fine structure change. At the interfacial layer, the Ti-L and O-K edges are very different (spectrum 2) and notably the O-K is not a combination / overlap of the  $\text{TiO}_2$  and  $\text{CeO}_2$  reference indicating that the electronic structure is locally different. We did not detect by EELS any diffusion of cerium into the  $\text{TiO}_2$  nanoparticles, either close to the ceria spheres or at

several tens of nanometers away. We estimate an upper substitution limit of ca. 0.25% of cerium substituted into Ti that might not be detected due to the lack of EELS sensitivity (see Fig S4.). Above STEM-EELS analysis demonstrates that with the formation of core-shell structure, not only a nanometric interfacial layer is induced but also the modification of the Ti valence of the  $\text{TiO}_2$  particles, where the range can be extended to 5–10 nm.

The overall valence change among these composites was then revealed by XAS. Fig. 5 (a) shows the Ti  $L_{3,2}$ -edge XANES spectrum of  $\text{TiO}_2$  and  $\text{TiO}_2@H\text{-CeO}_2$  composite with different molar ratio between Ti and Ce. In a rough description, the  $L_3$  and  $L_2$  edge further split into  $t_{2g}$  ( $d_{xy}$ ,  $d_{xz}$  and  $d_{yz}$ ) and  $e_g$  ( $d_{x^2-y^2}$  and  $3d_{z^2}$ ) because of the crystal field effect [25 26] and the observed  $L_3$  ( $e_g$ ) shoulder is typical of an anatase phase [24] in agreement with the EELS observation. The XAS on the Ce-3Ti has blurred fine structure while the shoulder is more visible for the Ce-7Ti, implying that with further  $\text{TiO}_2$  deposition results in NPs with lower  $\text{Ti}^{3+}$  contribution.

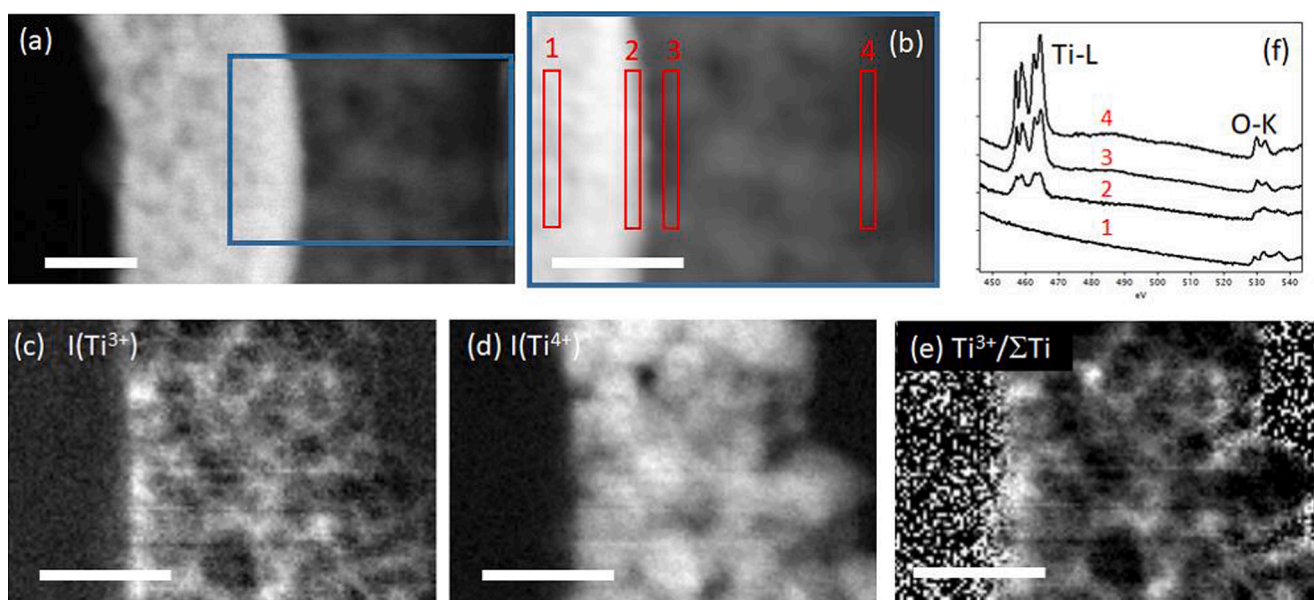


**Fig. 4.** (a,b) STEM-HAADF image of Ce-5Ti. The blue box indicates the area for EELS spectromicroscopy. The red boxes indicates positions where spectra have been extracted. (c, d, e) intensity of the EELS  $\text{Ti}^{3+}$ ,  $\text{Ti}^{4+}$  and  $\text{Ti}^{3+}/\Sigma\text{Ti}$  edges, (f) EELS Ti-L edges extracted from the red boxes. Boxes 1,2,3,4 are from the  $\text{CeO}_2$ , the interfacial layer, and the titania particles at different distance from the interface. All scale bars are 20 nm long.

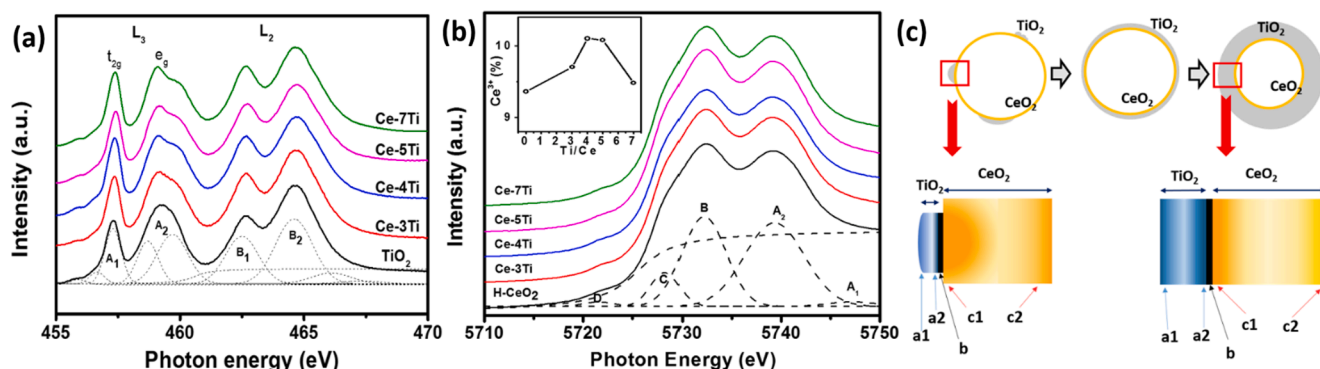


Fig. 5. XANES spectrum of (a) Ti-L edge and (b) Ce  $L_{3}$ -edge of  $\text{TiO}_2$ @H-CeO<sub>2</sub> composite with different Ti/Ce ratio.  $\text{Ce}^{3+}$  ratio obtained from the Ce  $L_{3}$ -edge is plotted in the inset figure. (c) Illustration of the variation trend of defect structure with changing the molar ratio of Ti to Ce. Area  $a_1$  and  $a_2$  present  $\text{Ti}^{3+}$  rich area in  $\text{TiO}_2$  shell. Area  $c_1$  and  $c_2$  are  $\text{Ce}^{3+}$  rich region of H-CeO<sub>2</sub>. Region  $c$  is the Ti-Ce-O interface layer formed during synthesis process.

XANES of Ce  $L_{3}$ -edge of H-CeO<sub>2</sub> and  $\text{TiO}_2$ @H-CeO<sub>2</sub> composites are demonstrated in Fig. 5 (b). Ce  $L_{3}$ -edge arise from the electron transition from  $2p_{3/2}$  to  $5d$  unoccupied state and can be used to estimate the charge state of Ce. All the spectrum were subtracted by an arctangent function to eliminate the background of the electron transition to continuum state and fitted by Gaussian functions. The amount of  $\text{Ce}^{3+}$  can be evaluated by  $I_c/I_{total}$ , where  $I_c$  is the area of the peak C and  $I_{total}$  is the sum of the area of peak A, B and C [27]. The estimated results are shown in the inset figure, showing that with increasing the ratio of Ti/Ce from 0 to 4, the concentration of  $\text{Ce}^{3+}$  was increased. However, the concentration of  $\text{Ce}^{3+}$  decreased with further enhance the Ti/Ce ratio to higher than 5. The variation trend of the valence of cations, including Ti and Ce, with the Ti/Ce ratio are consistent with EELS analysis and can be interpreted by the formation of both  $\text{TiO}_2$  shell and interfacial layer. As illustrated in Fig. 5 (c), it is seen that in addition to the intrinsic  $\text{Ce}^{3+}$  at the surface of H-CeO<sub>2</sub>, more  $\text{Ce}^{3+}$  will be induced at the interface area during the  $\text{TiO}_2$  deposition process. However, it is noted that the calcination process after the deposition of  $\text{TiO}_2$  will further change the amount and distribution of  $\text{Ce}^{3+}$ . As a result, the Ce-4Ti sample is an optimum for the presence of  $\text{Ce}^{3+}$  and then decrease a bit for Ce-5Ti.

### 3.2. Optical properties

The UV-vis absorption spectrum of the  $\text{TiO}_2$ @H-CeO<sub>2</sub> composites with different Ti/Ce ratios is shown in Fig. 6 (a). The results of H-CeO<sub>2</sub> was plotted together. It shows that after the deposition of  $\text{TiO}_2$ , the

absorption of the composites is extended to visible light region, in particular for Ce-4Ti and Ce-5Ti. The band gap ( $E_g$ ) of H-CeO<sub>2</sub> with different content of  $\text{TiO}_2$  deposition was estimated by using Tauc plot [28]. Plotting  $(\text{ohv})^{1/2}$  versus  $h\nu$  based on Fig. 6 (a) gives the extrapolated intercept corresponding to  $E_g$  value, as displayed in the inset. Upon  $\text{TiO}_2$  deposited on the surface of H-CeO<sub>2</sub>,  $E_g$  decreases rapidly from 2.98 eV to 2.87 eV. As the ratio of Ti/Ce is enhanced to higher than 4, the value of  $E_g$  is increased slightly. The variation trend of  $E_g$  with the Ti/Ce ratio can be interpreted by the change of defect concentration deduced from abovementioned TEM and EELS analysis. For instance, the slight band gap energy re-increase as the Ti/Ce ratio exceeds 4 is in line with the  $\text{Ce}^{3+}$  decrease for same composition. The narrowing of  $E_g$  also indicates the enhanced ability to absorb visible light.

PL spectrum of hollow CeO<sub>2</sub> spheres and  $\text{TiO}_2$ @H-CeO<sub>2</sub> are shown in Fig. 6 (b). Six apparent peaks were observed. Peak A at 400 nm might be attributed to the emission of the band gap transition [29]. Peak B and Peak C can be assigned to band edge free excitons of  $\text{TiO}_2$  and oxygen vacancies with two trapped electrons [30 31]. Peak D at 470 nm might be attributed to charge transfer transition of oxygen vacancy trapped electrons [14]. Peak E at 480 nm results from the recombination of charge carriers and peak F at 490 nm are associated with charge transfer transition from  $\text{Ti}^{3+}$  to oxygen anion in a  $\text{TiO}_6^{2-}$  complex [32 33]. It is noted that after forming core-shell structure, all the peaks decline which indicates the recombination of photo induced electron-hole pairs was inhibited. The present result is consistent with Liu's work that the existence of  $\text{Ti}^{3+}$  is beneficial to prolong the life time of photo induced

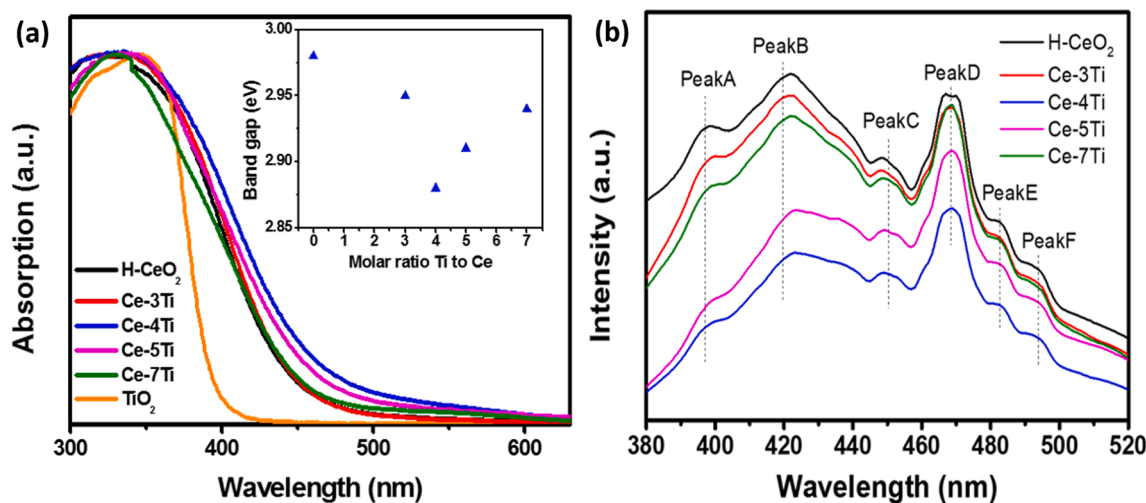


Fig. 6. (a) UV-vis spectrum for  $\text{TiO}_2$ , H-CeO<sub>2</sub> and  $\text{TiO}_2$ @H-CeO<sub>2</sub> composite and their band gap value (inset) (b) PL spectrum for H-CeO<sub>2</sub> and  $\text{TiO}_2$ @H-CeO<sub>2</sub> composite.

electron-hole pairs [34].

### 3.3. Photocatalyst performance

The photocatalyst activity of  $\text{TiO}_2@H\text{-CeO}_2$  composite was first evaluated by degrading MB under UV light irradiation. The degradation of MB was evaluated according to the change in the absorption of the final concentration ( $C$ ) divided by the initial concentration ( $C_0$ ) as a

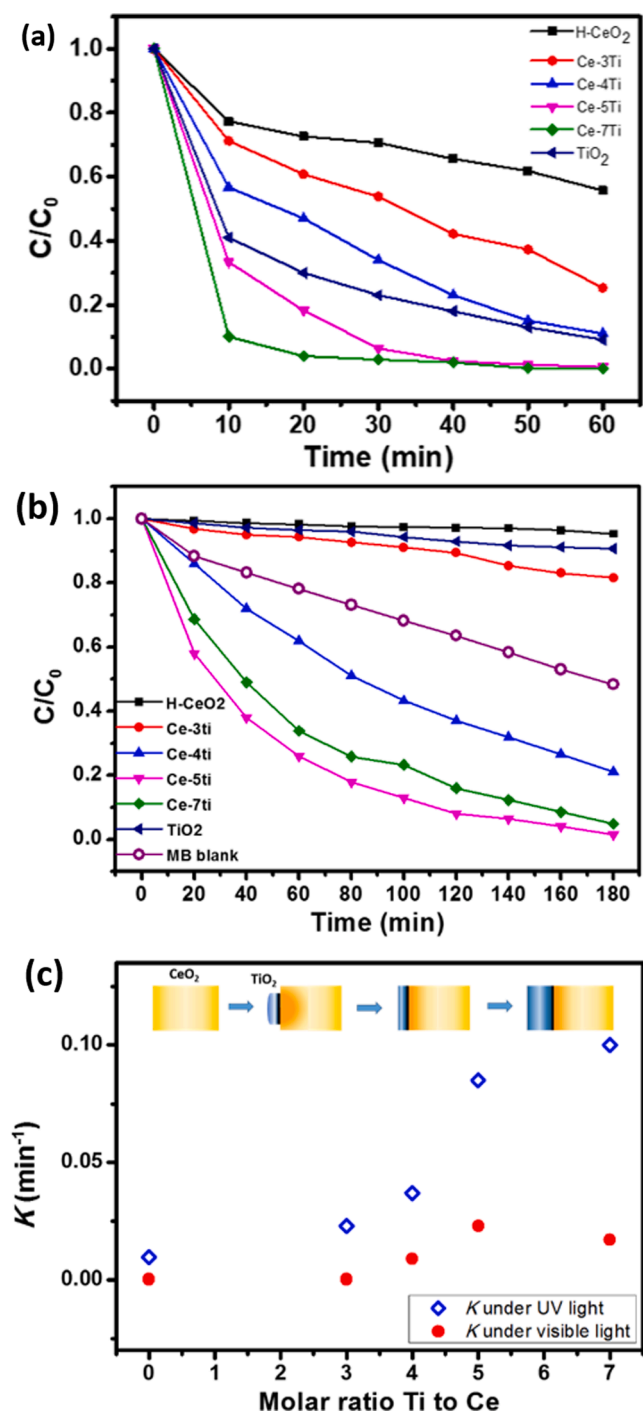


Fig. 7. Photocatalytic performances of  $H\text{-CeO}_2$  and  $\text{TiO}_2@H\text{-CeO}_2$  under (a) UV light and (b) visible light. Self degradation of MB under visible light is also plotted. (c) Rate constant  $K$  of  $\text{TiO}_2@H\text{-CeO}_2$  composites under UV light and visible light.  $K$  value of bare  $\text{TiO}_2$  NPs under UV light and visible light is 0.039 and  $5.42 \times 10^{-4} \text{ min}^{-1}$ , respectively. The variation of defect structure with changing the shell structure is illustrated in the insert.

function of irradiation time. The results are plotted in Fig. 7 (a). Enhanced photocatalyst activity was demonstrated. In Ce-7Ti, around 90% of MB was removed after 10 min irradiation, which is much better than that removed by bare  $\text{TiO}_2$  (~59%) and hollow  $\text{CeO}_2$  spheres (~22.7%). The photocatalytic activities of  $\text{TiO}_2@H\text{-CeO}_2$  composites under visible light irradiation are then evaluated and demonstrated in Fig. 7 (b). It is seen that in bare  $\text{TiO}_2$  nanoparticles and the as-prepared  $H\text{-CeO}_2$ , the photocatalytic ability is negligible. With the deposition of  $\text{TiO}_2$  shell, the photocatalytic ability is enhanced. However, it is noted that the degradation rate of MB in bare  $\text{TiO}_2$ , bare  $H\text{-CeO}_2$ , and Ce-3Ti is lower than that of MB blank. In samples with more complete core-shell structure, the photocatalyst effect is improved significantly. In Ce-5Ti and Ce-7Ti, the removal of MB could reach 90% after irradiation for 120 min.

The variation of photocatalytic performance among the composites was then interpreted by comparing the rate constant  $K$  which can be estimated by fitting a pseudo first order kinetic model.  $K$  value of bare  $\text{TiO}_2$  NPs under UV light and visible light is 0.039 and  $5.42 \times 10^{-4} \text{ min}^{-1}$ , respectively. As shown in Fig. 7 (c), it is seen that  $K$  value does not enhanced monotonously with rising the  $\text{TiO}_2$  content. Several trends are observed for the  $K$  values under UV light irradiation. It first increases gradually with the Ti/Ce ratio and then has an abrupt jump for a Ti/Ce ratio of 5. With further enhancing the Ti/Ce ratio, the slope is again reduced. The photodegradation rate reached for the Ce-7Ti is higher than that of hollow core/shell  $\text{CeO}_2@H\text{-CeO}_2$  [22] and is comparable to the yolk-shell structure of  $\text{TiO}_2@H\text{-CeO}_2$  reported by Yuan et al. [17] showing an overall good performance. The evolution of the  $K$  values under visible light irradiation has a different trend, exhibiting an optimum for a Ti/Ce ratio of 5. At that ratio, the  $K$  value is substantially higher than the reported  $\text{TiO}_2@H\text{-CeO}_2$  nanocubes, in which  $K$  value was only  $0.012 \text{ min}^{-1}$  [20].

As demonstrated in the microstructure analysis section, both the concentration and distribution of  $\text{Ce}^{3+}$  as well as  $\text{Ti}^{3+}$  strongly depend on the shell structure. With increasing the molar ratio of Ti to Ce, the amount and the coverage of  $\text{TiO}_2$  nanoparticles increase, which result in the enhancement of both  $\text{Ce}^{3+}$  and  $\text{Ti}^{3+}$  content at interface areas. Together with the intrinsic  $\text{Ce}^{3+}$  and  $\text{Ti}^{3+}$  at surface, the defect content reaches maximum as the molar ratio of Ti/Ce is close to 4. With further increase the content of Ti, the thick shell lead the decreasing of either  $\text{Ti}^{3+}$  or  $\text{Ce}^{3+}$ . Above trend of defect variation with changing the shell structure was illustrated in the insert figure in Fig. 7 (c).

As a consequence, abovementioned photocatalytic performance of  $\text{TiO}_2@H\text{-CeO}_2$  composites could be interpreted by the synergistic contribution from the surface of  $\text{TiO}_2$  NPs and the interface areas of  $\text{TiO}_2/\text{CeO}_2$ . With increasing the content of  $\text{TiO}_2$ , under UV light irradiation, both  $\text{CeO}_2$  and  $\text{TiO}_2$  can be excited to generate electron-hole pairs. Therefore, the photocatalytic performance was enhanced as increasing the surface area of  $\text{TiO}_2$  and the interface area of  $\text{TiO}_2/\text{CeO}_2$ . The jump is obtained when the  $\text{CeO}_2$  sphere was fully covered by  $\text{TiO}_2$  nanoparticles, maximizing the interface role. With further increasing the  $\text{TiO}_2$  shell thickness, the enhancement of photocatalytic performance becomes smaller since only contributed by  $\text{TiO}_2$  nanoparticles. On the other hand, only  $\text{CeO}_2$  with proper defect structure could be excited under visible light irradiation. In the bare  $\text{TiO}_2$  and the bare  $H\text{-CeO}_2$ , the defect content is low and the band gap energy is large, which could not provide advantage for the degradation of dye. Self degradation of MB has been observed before [35,36]. The poor degradation ability obtained in  $H\text{-CeO}_2$ ,  $\text{TiO}_2$  and Ce-3Ti than the blank sample may be due to the scattering of visible light by the added particles and the interference of the  $\text{CeO}_2$  surface state on the photodegradation process [37,38]. Small improvement observed in the Ce-3Ti might be associated to the induced  $\text{Ce}^{3+}$  at the surface layer. In Ce-5Ti, the optimum is obtained where  $\text{TiO}_2$  NPs fully covered the ceria and the complete interface is formed. Beyond the interfacial properties on the ceria (change in the recombination of photoinduced electron-hole pairs, ...), some of the remarkable performance observed under visible light might also be associated to the

reduced / defective TiO<sub>2</sub> located up to 5–10 nm from the interface. Obviously, further adding less defective TiO<sub>2</sub> (Ce-7Ti) do not benefit to the photo-degradation properties as expected from the low efficiency of TiO<sub>2</sub> under visible light irradiation.

#### 4. Conclusion

TiO<sub>2</sub>@H-CeO<sub>2</sub> with different Ti/Ce ratio was synthesized successfully by SP method followed by sol-gel process. By utilizing high resolution TEM and EELS, a thin defective interfacial oxide layer and the reduced TiO<sub>2</sub> surface was demonstrated, which is favorable to reduce the band gap and inhibit the recombination of photoinduced electron-hole pairs. Compared with bare TiO<sub>2</sub> NPs and CeO<sub>2</sub> hollow spheres, TiO<sub>2</sub>@H-CeO<sub>2</sub> composite exhibited the improved photocatalytic performance in MB. By optimizing the TiO<sub>2</sub> shell thickness, the highest photocatalytic activity was achieved, as shown in Ce-7Ti with  $K = 0.1 \text{ min}^{-1}$  under UV light and Ce-5Ti with  $K = 0.023 \text{ min}^{-1}$  under visible light.

#### CRedit authorship contribution statement

**Yi-Che Chen:** Formal analysis, Validation. **Yu-Cheng Chang:** Formal analysis, Validation. **Alexandre Gloter:** Methodology, Resources, Writing - review & editing. **Pei-Kai Hsu:** Formal analysis, Validation. **Jenn-Ming Song:** Conceptualization, Investigation, Resources. **Shih-Yun Chen:** Investigation, Conceptualization, Formal analysis, Writing - original draft, Writing - review & editing, Supervision, Project administration, Funding acquisition.

#### Declaration of Competing Interest

The authors declare that they have no known competing financial interests or personal relationships that could have appeared to influence the work reported in this paper.

#### Acknowledgement

The authors would like to thank the Ministry of Science and Technology of the Republic of China, Taiwan, for financially supporting this research under Contract No. MOST 107-2112-M-011 -002 -MY3.

#### Appendix A. Supplementary data

Supplementary data to this article can be found online at <https://doi.org/10.1016/j.apsusc.2021.150602>.

#### References

[1] G. Li, D. Zhang, J.C. Yu, *Phys. Chem. Chem. Phys.* 11 (2009) 3775–3782.

- [2] M. Tahir, N.S. Amin, *Applied Catalysis A, General* 467 (2013) 483–496.  
 [3] L. Wang, J. Ding, Y. Chai, Q. Liu, J. Ren, X. Liu, W.L. Dai, *Dalton Trans.* 44 (2015) 11223–11234.  
 [4] J. Gong, F. Meng, X. Yang, Z. Fan, H. Li, *J. Alloys. Compd.* 689 (2016) 606–616.  
 [5] S. Fang, Y. Xin, L. Ge, C. Han, P. Qiu, L. Wu, *Appl. Catal. B* 179 (2015) 458–467.  
 [6] J. Yu, Q. Xiang, M. Zhou, *Appl. Catal. B* 90 (2009) 595–602.  
 [7] L. Jiang, X. Yuan, Y. Pan, J. Liang, G. Zeng, Z. Wu, H. Wang, *Appl. Catal. B* 217 (2017) 388–406.  
 [8] T.K. Sau, A.L. Rogach, F. Jackel, T.A. Klar, J. Feldmann, *Adv. Mater.* 22 (2010) 1805–1825.  
 [9] O. Nicoletti, F. de la Pena, R.K. Leary, D.J. Holland, C. Ducati, P.A. Midgley, *Nature* 502 (2013) 80–84.  
 [10] X. Zhou, G. Liu, J. Yu, W. Fan, *J. Mater. Chem.* 22 (2012) 21337.  
 [11] J. Xie, D. Jiang, M. Chen, D. Li, J. Zhu, X. Lü, C. Yan, *Colloids Surf., A* 372 (2010) 107–114.  
 [12] N. Yan, Z. Zhu, J. Zhang, Z. Zhao, Q. Liu, *Mater. Res. Bull.* 47 (2012) 1869–1873.  
 [13] G.B. Vieira, H.J. José, M. Peterson, V.Z. Baldissarelli, P. Alvarez, R. de Fátima Peralta Muniz Moreira, *J. Photochem. Photobiol. A* 353 (2018) 325–336.  
 [14] J. Tian, Y. Sang, Z. Zhao, W. Zhou, D. Wang, X. Kang, H. Liu, J. Wang, S. Chen, H. Cai, H. Huang, *Small* 22 (2013) 3864–3872.  
 [15] M.J. Muñoz-Batista, M.N. Gómez-Cerezo, A. Kubacka, D. Tudela, M. Fernández-García, *ACS Catal.* 4 (2014) 63–72.  
 [16] Y. Liu, T. Li, W. Chen, Y. Guo, L. Liu, H. Guo, *RSC Adv.* 5 (2015) 11733–11737.  
 [17] B. Yuan, Y. Long, L. Wu, K. Liang, H. Wen, S. Luo, H. Huo, Ho. Yang, J. Ma, *Catal. Sci. Technol.* 6 (2016) 6396–6405.  
 [18] M. Ye, Q. Zhang, Y. Hu, J. Ge, Z. Lu, L. He, Z. Chen, Y. Yin, *Chem. Eur. J.* 16 (2010) 6243–6250.  
 [19] H. Zhang, M. Ying, R. Gao, L. Hu, Z. Jiao, X. Zhu, *RSC Adv.* 5 (2015) 58439–58448.  
 [20] F. Chen, P. Ho, R. Ran, W. Chen, Z. Si, X. Wu, D. Weng, Z. Huang, C. Lee, *J. Alloys. Compd.* 714 (2017) 560–566.  
 [21] Jiabai Cai, Wu. Xueqing, Shunxing Lia, Fengying Zheng, *Appl. Catal. B: Environ.* 201 (2017) 12–21.  
 [22] Lixin Zhang, Jia Zhang, Hongfang Jiu, Xia Zhang, Xu. Meiling, *J. Mater. Sci.* 50 (2015) 5228–5237.  
 [23] L. Zhang, J. Zhang, H. Jiu, X. Zhang, M. Xu, *J. Mater. Sci.* 50 (2015) 5228–5237.  
 [24] A. Gloter, C. Ewels, P. Umek, D. Arcon, C. Colliex, *Phys. Rev. B* 80 (2009), 035413.  
 [25] G.S. Henderson, X. Liu, M.E. Fleet, *Phys. Chem. Miner.* 29 (2002) 32–42.  
 [26] H.W. Kuo, C.J. Lin, H.Y. Do, R.Y. Wu, C.M. Tseng, K. Kumar, C.L. Dong, C.L. Chen, *Appl. Surf. Sci.* 502 (2020), 144297.  
 [27] S.Y. Chen, R.J. Chen, W. Lee, C.L. Dong, A. Gloter, *Phys. Chem. Chem. Phys.* 16 (2014) 3274–3281.  
 [28] F. Bensouici, M. Bououdina, A.A. Dakhel, R. Tala-Ighil, M. Tounane, A. Iratni, T. Souier, S. Liu, W. Cai, *Appl. Surf. Sci.* 395 (2017) 110–116.  
 [29] A.K. Tripathi, M.K. Singh, M.C. Mathpal, S.K. Mishra, Arvind Agarwal 549 (2013) 114–120.  
 [30] J. Tao, Z. Sun, Y. Cheng, M. Zhang, J. Lv, S. Shi, G. He, X. Jiang, X. Chen, X. Wang, Z. Wang, Z. Gong, *Sci. Rep.* 7 (2017) 5291.  
 [31] L. Kernazhitsky, V. Shymanovska, T. Gavrillo, V. Naumov, L. Fedorenko, V. Kshnyakin, J. Baran, *J. Lumin.* 146 (2014) 199–204.  
 [32] P. Parnicka, P. Mazierski, T. Grzyb, Z. Wei, E. Kowalska, B. Ohtani, W. Lisowski, T. Klimczuk, J. Nadolna, *J. Catal.* 353 (2017) 211–222.  
 [33] B. Choudhury, B. Borah, A. Choudhury, *Photochem. Photobiol.* 88 (2012) 257–264.  
 [34] Y. Liu, P. Fang, Y. Cheng, Y. Gao, F. Chen, Z. Liu, Y. Dai, *Chem. Eng. J.* 219 (2013) 478–485.  
 [35] Q. Zhao, X. Deng, M. Ding, L. Gan, T. Zhai, X. Xu, *Cryst. Eng. Comm.* 17 (2015) 4394.  
 [36] Y. Zhao, Q. Li, Y. Li, *Catalysts* 11 (2021) 327.  
 [37] J. Yao, C. Wang, *Int. J. Photoenergy* (2010), 643182.  
 [38] Q. Li, L. Song, Z. Liang, T. Wu, B. Huang, F. Luo, Y. Du, C.H. Yan, *Adv. Energy Sustainability Res.* 2 (2021), 2000063.